MDPI

Article

Start-Up Process of High-Speed Micro-Grooved Pumping Seal for New Energy Vehicles

Hanqing Chen [1,2,*], Ruqi Yan [3] (ORCID), Xianzhi Hong [4], Xin Bao [4] and Xuexing Ding [1,*]

1   School of Petrochemical Engineering, Lanzhou University of Technology, Lanzhou 730050, China
2   School of Mechanical Engineering, Lanzhou Petrochemical University of Vocational Technology, Lanzhou 730060, China
3   School of Chemistry and Chemical Engineering, Lanzhou Jiaotong University, Lanzhou 730070, China; yanruqima@126.com
4   Chengdu Yitong Seal Co., Ltd., Chengdu 610100, China; hongxianzhi@cdytseal.com (X.H.); baoxin@cdytseal.com (X.B.)
*   Correspondence: 181080706002@lut.edu.cn (H.C.); dingxxseal@126.com (X.D.); Tel.: +86-188-9348-6963 (X.D.)

Abstract: With the growing global demand for clean energy, new energy vehicles are a key focus in the automotive industry. This paper investigates the micro-grooved pumping seal used in such vehicles, using a custom Python computational programme to study the start-up behaviour of a non-contact oil–gas two-phase micro-grooved seal. The research explores the balance of forces during start-up, employing fractal theory for surface contact force calculations and solving the two-phase laminar Reynolds equation by the finite difference method. The results show that high-speed micro-grooved seals perform well under typical conditions for new energy vehicles. When film thickness is below a critical value, fractal dimension and characteristic length influence the initial thickness. Above the critical value, film thickness increases non-linearly with rotational speed, whereas the leakage rate decreases linearly. Critical rotational speed decreases non-linearly with the oil–gas ratio, peaking at an oil–gas ratio of 0.06. Both critical speed and leakage rate increase linearly and non-linearly with pressure and temperature, respectively. The study highlights the boundary-line where leakage transitions to pumping, providing valuable guidance for optimising seal design in new energy vehicles.

Keywords: micro-grooved pumping seal; micro-convex body contact; oil–gas two-phase flow; start-up process; sealing performance; new energy vehicle

1. Introduction

With the continuous growth in global demand for clean energy, new energy vehicles, including pure electric and hybrid vehicles, have become a primary focus of development in the automotive industry. As a core component of these vehicles, the electric drive system significantly impacts overall performance, efficiency, and reliability. However, the high-speed operation and complex working conditions of the electric drive system impose stringent requirements on sealing technology. In extreme working environments, such as high rotational speeds, two-phase fluids, and bidirectional rotation, traditional sealing technologies show significant shortcomings in preventing lubricant leakage, reducing friction losses, and maintaining system stability.

In recent years, micro-grooved pumping seal technology has gradually emerged to address these challenges. This technology, based on the fluid dynamic pressure effect, is a non-contact sealing method suitable for high-speed rotating equipment. Its unique micro-groove design generates a dynamic pressure effect at the sealing interface, significantly enhancing the seal's load-bearing capacity and overall reliability. Compared to traditional rubber skeleton oil seals [1,2] and polytetrafluoroethylene (PTFE) oil seals [3–5],

micro-grooved pumping seals perform exceptionally well under conditions of high rotational speed, heavy loads, and bidirectional rotation, showing great potential in the electric drive systems of new energy vehicles. Additionally, since electric motors typically operate at extremely high rotational speeds (progressing towards exceeding 40,000 rpm [6]), the stability and anti-reversal capability of the seal during start-up are crucial factors that determine the motor's lifespan and performance. Traditional sealing technologies have weaker anti-reversal capabilities, whereas micro-grooved pumping seals, with their bidirectional micro-groove design on the sealing surface, provide a more stable fluid dynamic pressure effect during start-up, significantly enhancing anti-reversal capability. The research and application of this technology not only help improve the reliability and lifespan of seals but also effectively reduce lubricant leakage and environmental pollution, representing the future direction of sealing technology for new energy vehicles. However, the dynamic behaviour of the sealing system during the start-up process directly affects its reliability and long-term stable operation. Therefore, in-depth research on the start-up process of micro-grooved pumping seals, particularly the changes in sealing performance during this phase, has become a critical problem that needs to be addressed.

When examining the flow field characteristics during the start-up process of mechanical seals, the morphology and contact behaviour of the sealing surface have a direct impact on fluid flow patterns. Greenwood and Williamson [7] proposed a classic model for studying the contact of nominally flat surfaces, providing a foundational theory for analysing mechanical seals and lubrication interfaces. Mandelbrot [8] suggested that fractal geometry could effectively describe complex random phenomena in nature, such as terrain undulations and coastline shapes, offering a new perspective on contact mechanics. Johnson [9] established a basic framework of contact theory, providing classical theoretical support for contact problems in lubrication and tribology. Majumdar and Bhushan [10] explored the role of fractal geometry in roughness characterisation and surface contact mechanics, proposing new methods for analysing surface roughness. Based on fractal geometry, Majumdar and Bhushan [11] developed a fractal model of elastic-plastic contact between rough surfaces, demonstrating its effectiveness in describing the relationship between surface roughness and contact behaviour. Wang and Komvopoulos [12] studied the interfacial temperature distribution under slow sliding conditions using fractal theory, concluding that fractal models can effectively describe thermal transfer behaviour at contact interfaces, and revealing the impact of thermal coupling on friction performance. Dong and Zhang [13] refined the M-B elastic-plastic contact model, finding that it more accurately reflects actual operating conditions when describing the elastoplastic contact behaviour of rough surfaces. Ge and Zhu [14] highlighted the significant potential of fractal theory in tribology for optimising friction behaviour under complex conditions. Bhushan [15,16] further investigated the application of fractal geometry in surface roughness characterisation, evaluated the measurement capabilities of different experimental techniques for real contact areas, and proposed new experimental methods to improve measurement accuracy. Wei et al. [17] developed a sliding friction surface contact mechanics model based on fractal theory, analysing the impact of rough surfaces on friction performance and suggesting the optimisation of friction interface design through fractal models. Ding et al. [18] constructed a rough surface contact model based on fractal theory, analysing the impact of different base lengths on sealing interface performance and proposing design solutions to enhance sealing performance. Zhao et al. [19] proposed a prediction model for mechanical seal leakage rate and film thickness based on fractal contact theory, suggesting that optimising these parameters can significantly improve the reliability and lifespan of seals.

In addition to surface contact characteristics, lubrication and dynamic pressure effects at the microscale are crucial factors influencing sealing performance. Fukui and Kaneko [20], through their analysis of the lubrication mechanism of ultra-thin gas films, proposed a generalised lubrication equation, which they believe is significant for the design of microscale lubrication systems. Gu [21] highlighted that the lift-off phenomenon and lift characteristics of the sealing face in mechanical face seals significantly affect the stability

and lifespan of the seal. Li et al. [22] emphasised that the opening characteristics of dry gas seals are critical for enhancing sealing effectiveness, particularly during the start-up process, where the lift-off phenomenon of the sealing face directly impacts the control of working pressure. Fan et al. [23] investigated the start-up process of dry gas seals under steam lubrication conditions and found that steam lubrication can effectively improve the start-up performance of seals, particularly in high-humidity environments. Sun et al. [24] analysed the impact of seal ring material properties and surface topography on the dynamic contact characteristics of dry gas seals during start/stop phases, providing recommendations for optimising sealing performance.

While fractal geometry models and contact mechanics have made significant progress in describing microscopic surface contact behaviour, existing models are often applied under steady-state conditions, and their impact on the dynamic response of micro-grooved pumping seals during the start-up phase has not been fully explored. As a result, there is still a lack of research combining fluid dynamic pressure effects with fractal contact models during the start-up process, particularly in the transient behaviour analysis of seals under high rotational speeds, two-phase flow, and bidirectional rotation conditions. This gap represents a critical bottleneck limiting the broader application of this technology.

Considering this background, this study focused on analysing the changes in the sealing performance of high-speed micro-grooved pumping seals for new energy vehicles during the start-up process. Before the separation of the end faces, the research applied tribology and contact mechanics as foundational theories, with fractal geometry models used to describe the contact behaviour of microscopic surfaces. This approach explored the influence of surface contact microstructures and contact characteristics on sealing performance. After the separation of the end faces, the study employed the compressible steady-state two-phase laminar Reynolds equation, incorporating real gas effects. The virial and Lucas equations were utilised to describe changes in real gas effects and viscosity, respectively, while the oil–gas ratio was introduced to determine the equivalent density and equivalent viscosity. Utilising numerical simulations, the study investigated the dynamic pressure effects under transient start-up conditions and their impact on sealing performance, addressing gaps in existing research. These innovative investigations will not only enhance the understanding of the start-up process of micro-grooved pumping seals but also provide essential theoretical foundations and practical insights for the sealing design of electric drive systems in future new energy vehicles.

2. Theoretical Framework

2.1. Geometric Framework

The micro-grooved pumping seal structure for new energy vehicles is shown in Figure 1. The rotating ring is made of silicon carbide, while the stationary ring is crafted from graphite, with grooves etched onto the rotating ring. The rotating ring is secured within the rotating ring seat, which is positioned relative to the shaft using a pin and sealed with an O-ring. On the opposite side, the stationary ring is connected to the sealing cover via a bellows (wave spring), which serves both as an elastic element and a seal. The sealing cover is further sealed to the sealing chamber with a gasket. During operation, the micro-grooved pumping seal allows the oil–gas mixture to enter from the low-pressure side, where it is pumped through the dynamic pressure grooves on the sealing face to the high-pressure side. This creates an ultra-thin oil–gas two-phase film on the sealing face, effectively achieving zero oil and gas leakage. When the system is shut down, the sealing faces close, preventing lubricant leakage and ensuring a tight seal. This is a new type of seal [25].
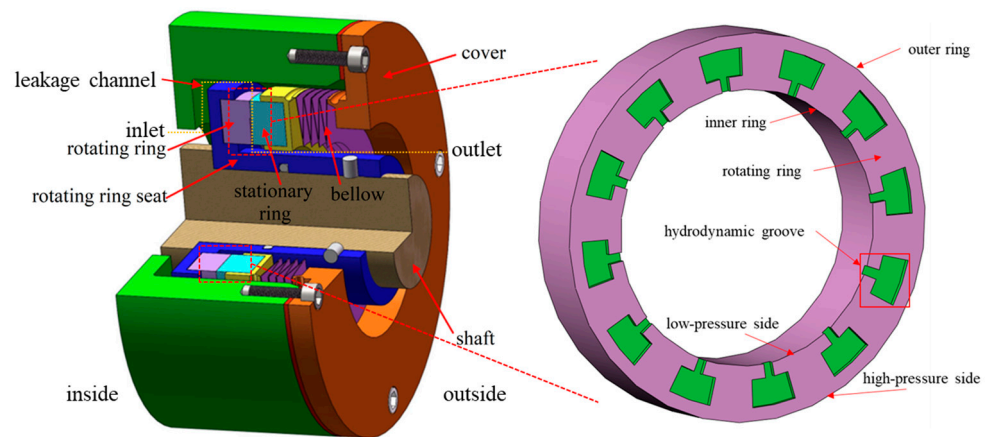
Figure 1. Schematic of proposed micro-grooved pumping seal for new energy vehicles.

2.2. Force Balance During the Start-Up Process

As shown in Figure 2, various forces, such as spring force, fluid static pressure, fluid dynamic pressure, and surface contact force, act on the sealing rings during the start-up of this new type of seal for new energy vehicles. These forces balance each other, collectively determining the relative position of the two sealing rings. Regardless of whether the sealing faces are rotating relative to each other or stationary, the closing force is always present. This force is generated partly by the pressure acting on the non-contacting back area of the sealing ring and partly by the spring pressure. At the initial stage of start-up, or when the two sealing faces are stationary, the end faces of the rotating and stationary rings, which have a certain surface roughness, experience micro-convex body contact. The interaction between these micro-convex bodies generates the surface contact force. During the start-up process, in addition to the surface contact force, fluid dynamic pressure is generated by the oil–gas mixture under the influence of the hydrodynamic grooves. At this stage, the surface contact force and fluid dynamic pressure together create the opening force. As the rotational speed increases, the two sealing faces gradually separate due to the fluid dynamic pressure, and eventually, the opening force is entirely sustained by the fluid dynamic pressure, referred to as the film opening force.
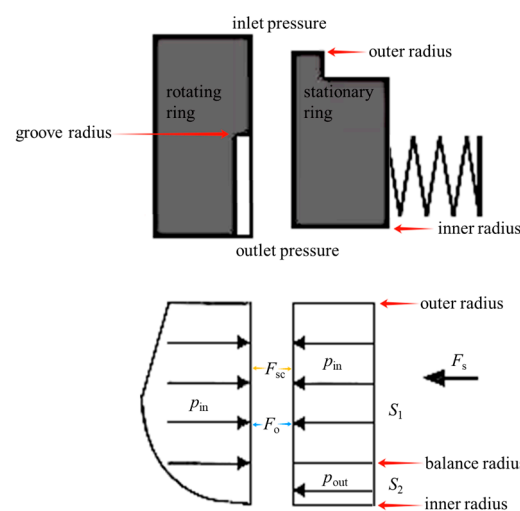

Figure 2. Schematic of the balance of forces.

The closing force is composed of the fluid static pressure and the spring force acting on the sealing ring. Typically, the spring force varies with the compression length in its calculation formula. However, since the compression length in this study is at the micron

level, the variation in spring force is negligible and can be considered constant. As a result, the spring force is treated as a fixed value in this study.

The formula for calculating the closing force is:

$$F_c = S_1 \cdot (p_{in}) + S_2 \cdot (p_{out}) + F_s \tag{1}$$

where S_1 is the high-pressure side surface area of the back of the sealing ring (in m^2); p_{in} is the inlet pressure (i.e., the gas pressure at the outer radius of the sealing ring, the high-pressure side, in Pa); S_2 is the low-pressure side surface area of the back of the sealing ring (in m^2); p_{out} is the outlet pressure (i.e., the gas pressure at the inner radius of the sealing ring, the low-pressure side, in Pa); and F_s is the spring force (N).

During the start-up process, the sum of the surface contact force and the film opening force equals the closing force, but they have an inverse relationship. As the film opening force increases, the surface contact force decreases, and vice versa. The force balance relationship during the start-up process is as follows:

$$F_c = F_{sc} + F_o \tag{2}$$

where F_c is the closing force (N), F_{sc} is the surface contact force (N), and F_o is the film opening force (N).

2.3. Critical States During the Start-Up Process

During the start-up process, initially, the two sealing faces are at rest relative to each other. As the rotational speed gradually increases, the faces transition from initial contact and friction to being finally separated by the fluid's hydrodynamic pressure. The "critical state" refers to the boundary condition during start-up, where the faces transition from contact to non-contact.

2.3.1. Critical Film Thickness h_c

The critical film thickness is a dimensional threshold. When the film thickness is below this critical film thickness, it falls under mixed friction [21]; when it exceeds the critical film thickness, it transitions to fluid friction, which, in this study, is also referred to as oil–gas two-phase flow lubrication. When the film thickness is less than the critical film thickness, the rotating and stationary end faces have not fully separated. At this stage, both oil–gas two-phase lubrication and surface contact are present. Therefore, when the film thickness is below the critical film thickness, the film opening force consists of the fluid dynamic pressure from the oil–gas two-phase film and the surface contact force from the micro-convex bodies on the rough surfaces of the sealing faces. Gu [21] referred to the critical film thickness as the contact film thickness, which represents the critical point wherein mixed friction transitions to fluid friction. It can be expressed as:

$$h_c = 3.75 \cdot \sqrt{R_{a1}^2 + R_{a2}^2} \tag{3}$$

where R_{a1} and R_{a2} are the surface roughness of the harder and softer materials, respectively (in m).

According to the "specification for dry gas seal" [26], $R_{a1} \leq 0.1$ μm and $R_{a2} \leq 0.2$ μm; thus, the maximum critical film thickness is $h_c \approx 0.85$ μm under these conditions.

2.3.2. Critical Rotational Speed n_c

The critical rotational speed represents the threshold for force balance: below this speed, the surface contact force and film opening force together balance the closing force, while above it, only the film opening force balances the closing force. When the gap between the rotating and stationary rings reaches the critical film thickness, the rotational speed of the rotating ring causes the oil–gas two-phase film to generate a film opening force that balances the closing force, resulting in a surface contact force of zero. This

speed is known as the critical rotational speed. Once the rotational speed exceeds the critical rotational speed, the film opening force increases. When the film opening force surpasses the closing force, the film thickness also increases, exceeding the critical film thickness. As the film thickness increases, the film opening force decreases. When the film opening force decreases sufficiently to balance the closing force, the film thickness stabilises or fluctuates slightly around the new equilibrium value. This is a dynamic equilibrium process, simplified here as a quasi-static equilibrium process. Thus, as the rotational speed continues to increase, the rotating and stationary rings reach new equilibrium positions, with the film thickness continually increasing to maintain the balance between the film opening force and the closing force. With a constant closing force, the critical rotational speed is influenced by factors such as inlet pressure, oil–gas ratio, and temperature. The purpose of this study is to explore how these factors affect the critical rotational speed and to optimise performance parameters during the start-up process of this new type of seal for new energy vehicles.

2.4. Rough Surface Contact

2.4.1. Surface Contact Process

Due to the roughness of the sealing end faces, when the device is stationary and the two sealing faces are in contact, or during the initial stage of start-up, a portion of the surfaces remains in contact. The contact of rough surfaces can be described using fractal contact theory. Since the rotating and stationary rings of this new type of seal involve a combination of a hard and a soft ring, the contact analysis of the sealing friction interface can be simplified to the interaction between an ideal rigid smooth surface and a rough surface, as illustrated in Figure 3. Under the applied load F_{sc}, the rigid surface moves in the negative direction along the z-axis, and the micro-convex bodies sequentially undergo plastic, elastoplastic, and elastic contact states [27].
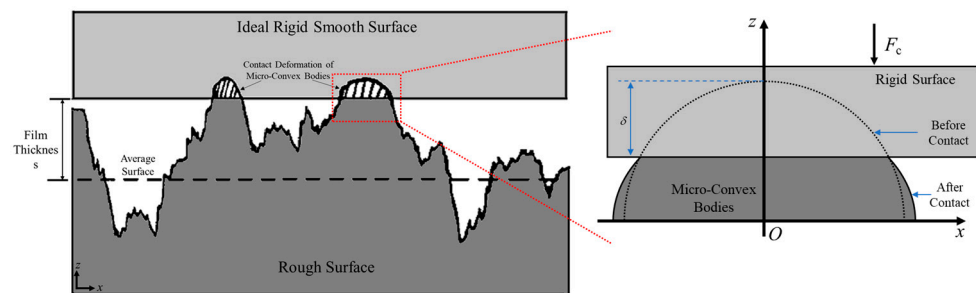

Figure 3. Contact deformation diagram of rough surface micro-convex body.

The normal deformation of the micro-convex bodies can be represented by the normal displacement, which is related to the maximum contact area of the micro-convex bodies on the contact surface. This relationship can be expressed as follows:

$$\begin{cases} \delta = G^{(D-1)} \cdot a_1^{(2-D)/2} \\ a_1 = \frac{2-D}{D} \cdot \psi^{(D-2)/2} \cdot A_r \\ \psi = 5.4532 \exp\left(\frac{-D}{0.62782}\right) + 1.499 \end{cases} \tag{4}$$

where δ is the normal displacement (in m); G is the characteristic length scale (in m); D is the fractal dimension (dimensionless); a_1 is the maximum contact area of the micro-convex bodies (in m^2); ψ is the area expansion coefficient (dimensionless); and A_r is the real contact area (in m^2).

The analysis clearly demonstrates that comprehending the correlation between the real area of contact and the surface contact force enables the determination of the relationship between the surface contact force and the normal displacement.

2.4.2. Surface Contact Force

The interaction force between rough surfaces is referred to as the surface contact force. It can be calculated using rough surface contact models based on statistical or fractal parameters. According to the fractal contact theory, the relationship between the real contact area and the surface contact force is as follows [14]:

$$
F_{sc} = \begin{cases} \frac{4}{3}\sqrt{\pi}E \cdot A_a \cdot G^{*D-1} \cdot g_1(D) \cdot \psi^{\frac{(D-2)^2}{4}} \cdot A_r^{*\frac{D}{2}} \cdot \left[\left(\frac{2-D}{D} \cdot \psi^{\frac{D-2}{2}} \cdot A_r^* \right)^{\frac{3-2D}{2}} - a_c^{*\frac{3-2D}{2}} \right] & D \neq 1.5 \\ \qquad\qquad\qquad +K \cdot \sigma_y \cdot A_a \cdot g_2(D) \cdot \psi^{\frac{(D-2)^2}{4}} \cdot A_r^{*\frac{D}{2}} \cdot a_c^{*\frac{2-D}{2}} & \\ 3^{-\frac{3}{4}}\sqrt{\pi}E \cdot A_a \cdot G^{*\frac{1}{2}} \cdot \psi^{\frac{1}{16}} \cdot A_r^{*\frac{3}{4}} \cdot \ln \left(\frac{A_r^*}{3\psi^{\frac{1}{4}} \cdot a_c^*} \right) + 3^{\frac{1}{4}}K \cdot \sigma_y \cdot A_a \cdot \psi^{\frac{1}{16}} \cdot A_r^{*\frac{3}{4}} \cdot a_c^{*\frac{1}{4}} & D = 1.5 \end{cases}
$$

(5)

where:

$$
\begin{cases} g_1(D) = \frac{D}{3-2D} \cdot \left(\frac{2-D}{D} \right)^{\frac{D}{2}} \\ g_2(D) = \left(\frac{D}{2-D} \right)^{\frac{2-D}{2}} \\ a_c = G^2 \cdot \left(\frac{\pi E^2}{225\sigma_y^2} \right)^{\frac{1}{D-1}} \\ E = \left[\frac{1-v_1^2}{E_1} + \frac{1-v_2^2}{E_2} \right]^{-1} \\ G^* = \frac{G}{\sqrt{A_a}} \\ A_r^* = \frac{A_r}{A_a} \\ a_c^* = \frac{a_c}{A_a} \end{cases}
$$

(6)

where σ_y is the yield strength of the softer material (in Pa); v_1 and v_2 are the Poisson's ratios of the harder and softer materials, respectively (dimensionless); E_1 and E_2 are the elastic moduli of the harder and softer materials, respectively (in Pa); E is the equivalent elastic modulus (in Pa); A_a is the nominal contact area (in m^2); a_c is the critical contact area (in m^2); and $g_1(D)$, $g_2(D)$, G^*, A_r^*, a_c^*, and K are detailed in reference [14].

2.5. Performance Parameters of Oil–Gas Two-Phase Film

2.5.1. Equation for Pressure Control

The fluid within the seal was presumed to be a Newtonian fluid exhibiting a zero-pressure gradient in the direction of film thickness. The deformation of the seal end surface was considered minimal, and temperature changes inside the flow field were not taken into account. Therefore, the steady-state Reynolds equation for the laminar flow field in this new type of seal can be given as follows [28,29]:

$$
\frac{1}{r} \cdot \frac{\partial}{\partial \theta} \left(\frac{\rho_e \cdot h^3}{12 \cdot \eta_e} \cdot \frac{\partial p}{\partial \theta} \right) + \frac{\partial}{\partial r} \left(\frac{r \cdot \rho_e \cdot h^3}{12 \cdot \eta_e} \cdot \frac{\partial p}{\partial r} \right) = r \cdot \omega \cdot \frac{\partial}{\partial \theta} (\rho_e \cdot h)
$$

(7)

where p, r, θ, ω, h, ρ_e, η_e, and the detailed calculation process of Equation (7) are provided in reference [25].

2.5.2. Steady-State Performance Metrics

By resolving the Equation (7), the opening force (F_o) and leakage rate (Q_m) can be obtained as follows:

$$
F_o = \int_0^{2\pi} \int_{r_i}^{r_o} p \cdot r \mathrm{d}r \mathrm{d}\theta
$$

(8)

and the leakage mass rate is:

$$
Q_m = \int_0^{2\pi} \int_0^h \rho_e \cdot u_r \cdot r \mathrm{d}z \mathrm{d}\theta
$$

(9)

3. Results and Discussion

The pressure control problem was numerically solved using the finite difference method, taking into account the impacts of real gas as well as the equivalent density and viscosity of the oil–gas two-phase mixture. The pumping mechanism and sealing properties were further analysed and commented. The geometric configuration and specifications of this new type of seal (which is an inverted trapezoidal groove in this work), as well as the operational circumstances and material characteristics, are presented in Figure 4, Table 1, Table 2, and Table 3, respectively. Figure 5 is the technical roadmap, where the "fluid dynamic pressure model" is based on reference [25].
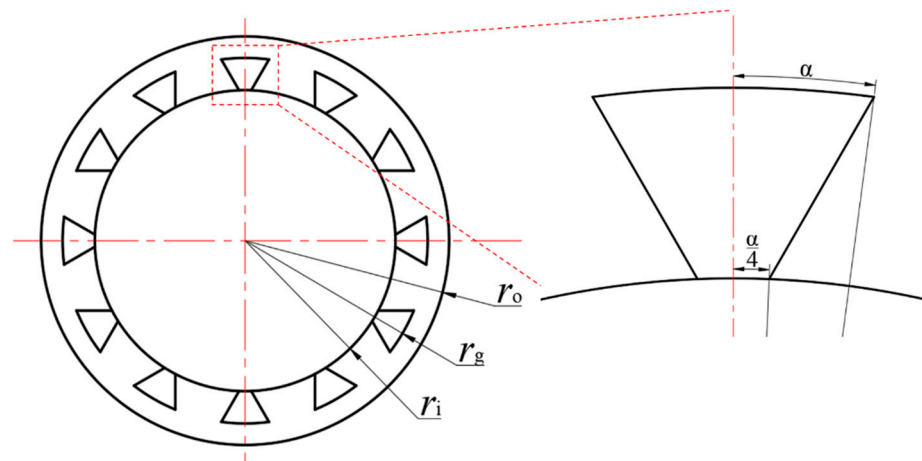

Figure 4. Schematic of dynamic ring size parameters.

Table 1. Geometric parameters of high-speed micro-groove pumping seal for new energy vehicles.

Parameter	Value
Outer radius r_o/mm	38
Inner radius r_i/mm	28
Number of grooves N_g	12
Groove depth h_g/μm	5
Groove root radius r_g/mm	34
Expanding angle of groove α/°	$180/(2 \cdot N_g)$

Table 2. Operating conditions parameters of high-speed micro-groove pumping seal for new energy vehicles.

Parameter	Value
Rotational velocity n/rpm	0~20,000
Inlet gauge pressure p_i/kPa	0~300
Outlet gauge pressure p_o/kPa	0
Inlet temperature T_i/°C	40~130
Outlet temperature (environmental) T_o/°C	20
Oil–gas ratio c	0.01~0.1
Spring force F_s/N	49

The parameters used in the calculation are all listed in Tables 1 and 2, which include $p_i = 0.1$ MPa, $T_i = 100$ °C, $n = 20000$ rpm, and an oil–gas ratio of 0.03, employing a Python programme. A Python programme I developed was employed, which contains all the detailed information regarding grid size, boundary conditions, and convergence criteria [25]. Figure 6 demonstrates the effect of grid density, utilising a grid count of 19,716 for this analysis.

Table 3. Material characteristic parameters of high-speed micro-groove pumping seal for new energy vehicles.

Parameter	Silicon Carbide Ring	Graphite Ring
Elastic modulus, E/GPa	400	20
Poisson's ratio, ν	0.14	0.24
Yield strength, σ_y/MPa	—	200
Fractal dimension D	—	1.6
Characteristic length scale G/m	—	6.7×10^{-9}
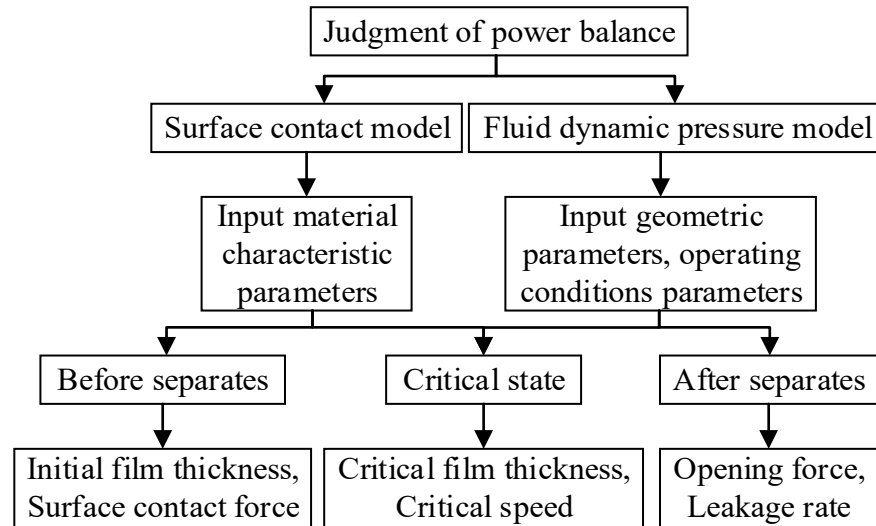
Figure 5. Technical roadmap.
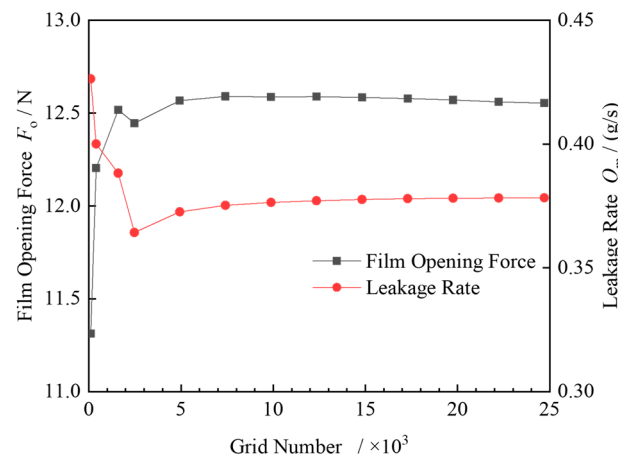
Figure 6. The effect of grid density.

3.1. Relationship Between Surface Contact Force and Film Opening Force During the Start-Up Process

By substituting the parameters from Tables 1 and 3 into Equations (4) and (5), the variations in surface contact force, film opening force, and film thickness were calculated. The blue dashed auxiliary lines in Figure 7 indicate the initial film thickness and critical film thickness under the operating conditions of this study.
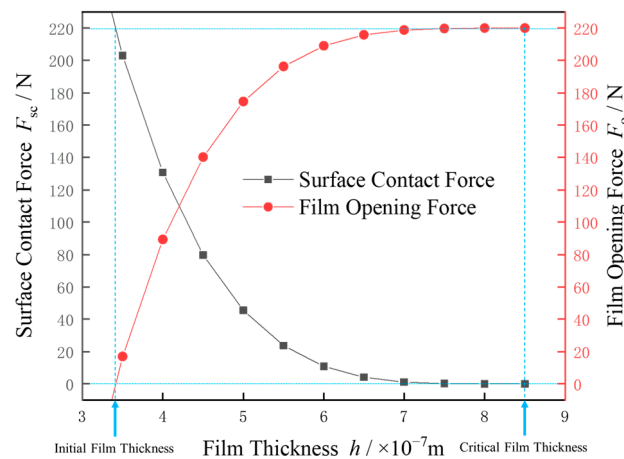
Figure 7. Relationship between surface contact force, film opening force, and film thickness.

According to Figure 7, the surface contact force decreases non-linearly as the film thickness increases. Conversely, as the film thickness decreases from the critical film thickness to zero, the surface contact force increases, and the rate of this increase also rises. According to Equation (2), the sum of the surface contact force and the film opening force always equals the closing force. When the surface contact force equals the closing force, the film opening force is zero, and the two sealing end faces are relatively stationary. At this point, the film thickness corresponds to the initial film thickness. When the surface contact force is zero and the film opening force equals the closing force, the rotational speed corresponds to the critical rotational speed, and the corresponding film thickness is the critical film thickness.

3.2. Influence of Fractal Parameters on Initial Film Thickness

The distance between the critical film thickness and the initial film thickness represents the maximum normal displacement of the micro-convex bodies. By varying the fractal dimension and characteristic length scale in the fractal contact model, it is conceivable to comprehend how variations in surface microtopography affect the initial film thickness.

3.2.1. Influence of Fractal Dimension

Using the parameters from Tables 1–3, and keeping the characteristic length scale constant, the relationship between the fractal dimension and the initial film thickness was calculated. As shown in Figure 8, the blue dashed auxiliary lines indicate the initial film thickness for various fractal dimensions.
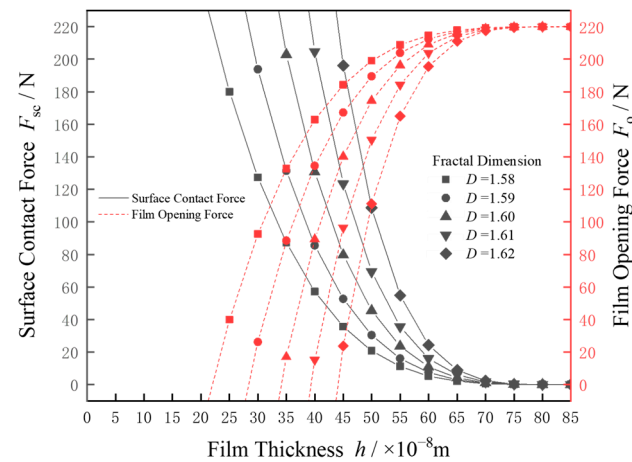

Figure 8. Initial film thickness under different fractal dimensions.

Figure 8 shows that the initial film thickness increases with the fractal dimension, but the rate of increase gradually diminishes. Alternatively, this can be interpreted as a decrease in the maximum normal displacement of the micro-convex bodies. This occurs because, as the fractal dimension increases, the self-similarity of the microstructure enhances significantly, making the surface structure more complex and detailed. The number of micro-convex bodies increases, expanding the effective contact area and dispersing the normal force. Consequently, the increased complexity of the micro-convex body shapes reduces the concentration of normal displacement, thereby improving the average deformation resistance of the micro-convex bodies. This leads to superior mechanical performance of the overall structure.

3.2.2. Influence of Characteristic Length Scale

Using the parameters from Tables 1–3, and keeping the fractal dimension constant, the relationship between the characteristic length scale and the initial film thickness was calculated. As shown in Figure 9, the blue dashed auxiliary lines indicate the initial film thickness for various characteristic length scales.
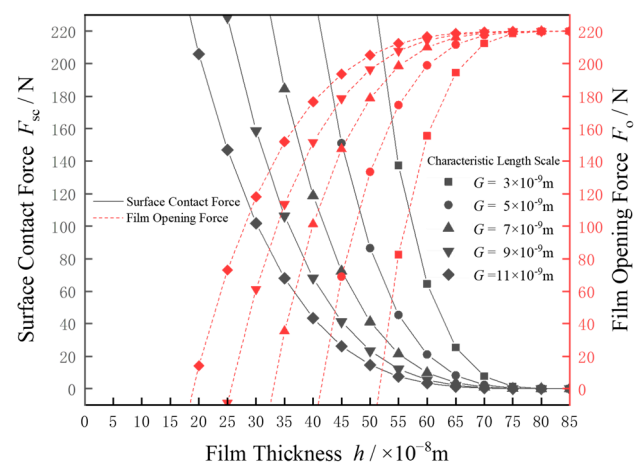

Figure 9. Initial film thickness under different characteristic length scales.

Figure 9 shows that the initial film thickness decreases as the characteristic length scale increases, with the rate of decrease gradually diminishing. This indicates that the maximum normal displacement of the micro-convex bodies increases. As the characteristic length scale increases, larger protrusions and depressions on the surface become more pronounced, leading to increased surface roughness. Additionally, the leakage channels and porosity between the contact surfaces may expand, affecting sealing performance and increasing the risk of leakage. Although the closing force remains constant, changes in surface topography cause uneven pressure distribution within the contact area, resulting in more significant local deformation of some micro-convex bodies during contact. Consequently, the normal displacement of the micro-convex bodies becomes larger, leading to a smaller initial film thickness.

The observations from the previous two sections indicate that changes in the fractal dimension and characteristic length scale significantly impact the initial film thickness during the start-up process of this new type of seals for new energy vehicles. By optimising the micro-structure and reducing contact porosity, the sealing performance of this new type of seal can be effectively enhanced, both when stationary and before separation. This research provides important guidance for material selection and surface treatment processes, thereby reducing the risk of leakage during the start-up process.

3.3. Analysis of Rotational Speed, End Face Gap, and Leakage After Separation

Utilizing the data from both Tables 1 and 2 for an input with a gauge pressure of 100 kPa, a temperature setting of 100 °C, and an oil–gas ratio of 0.03, the fluctuations in film

thickness and leakage rate were computed as the rotating speed progressively increased from 0 to 20,000 r/min. The findings are illustrated in Figure 10.
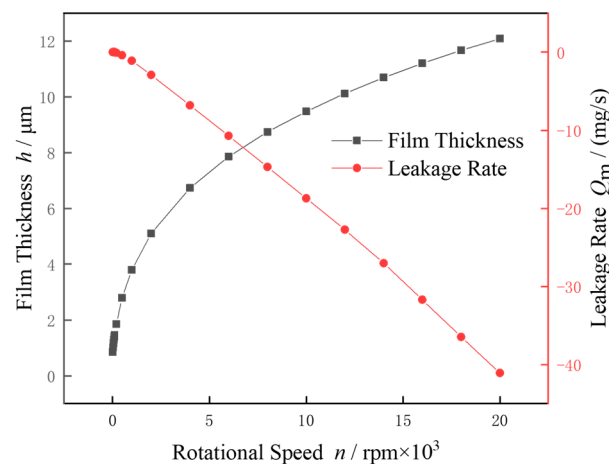

Figure 10. Film thickness and leakage rate at different rotational speeds.

Figure 10 shows that the film thickness increases non-linearly with rotational speed, rising rapidly at first and then more gradually. This trend indicates that the stiffness of the oil–gas two-phase film continuously decreases. Although increasing the rotational speed enhances the film opening force, the force balance relationship dictates that the film opening force is always balanced by the closing force, both of which remain constant. Therefore, as the rotational speed increases, the film thickness continues to increase until the forces reach a new balance. The continuously increasing film thickness, combined with the constant film opening force, results in a decrease in stiffness.

The leakage rate changes almost linearly with the rotational speed. It is important to note that the seal chamber serves as the inlet, while the environment acts as the outlet. When the sign of the leakage rate is positive, it indicates that the leakage direction flows from the inlet to the outlet, meaning that oil and gas are leaking from the sealed leakage channel to the outside, i.e., oil–gas leaks from the seal chamber into the environment. Conversely, a negative leakage rate means the flow is from the outlet to the inlet, i.e., from the environment into the seal chamber, referred to as the pumping rate. Therefore, as the rotational speed increases, the sealing system transitions from leakage to pumping. The rotational speed at which this transition occurs is called the boundary-line speed between leakage and pumping, which is approximately 102 r/min under these operating conditions.

3.4. Influence of Operating Condition Changes on Critical States

By altering various operating parameters, changes in the critical rotational speed were observed when the critical film thickness was set to 0.85 μm. Additionally, the performance parameters at this critical rotational speed were examined, with particular emphasis on the leakage rate.

3.4.1. Influence of Oil–Gas Ratio on Start-Up Performance

Applying the data from both Tables 1 and 2 for an inlet with a gauge pressure of 100 kPa, a temperature setting of 100 °C, and an oil–gas ratio incrementally increasing from 0.01 to 0.1, the variations in critical rotational speed and leakage rate were calculated. The results are presented in Figure 11.

Figure 11 shows that the critical rotational speed decreases non-linearly as the oil–gas ratio increases. This is because, as the oil–gas ratio increases, the equivalent density and viscosity of the oil–gas two-phase mixture also increase. As a result, a lower rotational speed is sufficient to generate the same film opening force and achieve the same critical film thickness.
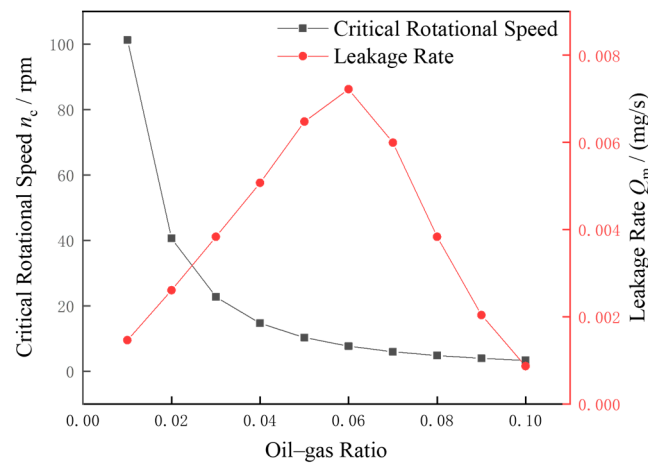
Figure 11. Critical rotational speed and leakage rate at different oil–gas ratios.

At different critical states corresponding to various oil–gas ratios, the leakage rate initially increases and then decreases non-linearly, peaking at an oil–gas ratio of approximately 0.06. According to previous research [25], when the rotational speed is constant, an increase in the oil–gas ratio increases the pumping rate, thereby reducing the leakage rate. Similarly, when the oil–gas ratio is constant, an increase in rotational speed decreases the leakage rate. Figure 11 highlights a special operating point during the start-up process: when the oil–gas ratio is approximately 0.06, the leakage rate is relatively high, either during start-up or during sustained low-speed operation after start-up. This suggests that in seal design, it is advisable to avoid an oil–gas ratio near 0.06. If an oil–gas ratio near 0.06 offers significant advantages in other performance aspects, it is crucial to minimise the number of start-stop cycles, accelerate quickly after start-up to reduce low-speed operation time, and limit the minimum rotational speed after start-up to effectively reduce the leakage rate.

3.4.2. Influence of Inlet Gauge Pressure on Start-Up Performance

Using the parameters from Tables 1 and 2, with an oil–gas ratio of 0.03, a temperature of 100 °C, and an inlet gauge pressure incrementally increasing from 0 to 300 kPa, the variations in critical rotational speed and leakage rate were calculated. The results are presented in Figure 12.
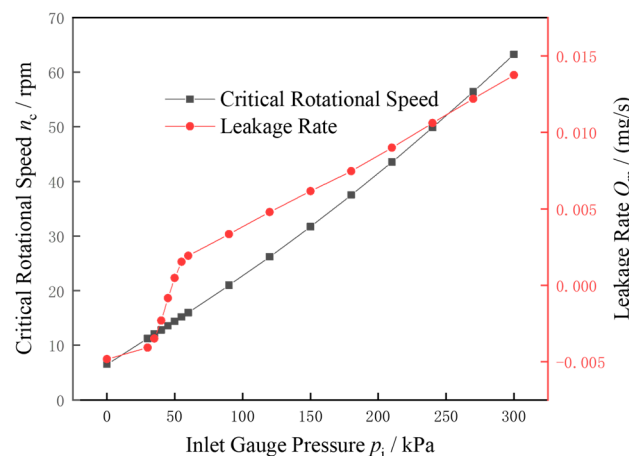

Figure 12. Critical rotational speed and leakage rate at different inlet gauge pressures.

Figure 12 shows that the critical rotational speed increases approximately linearly with the inlet gauge pressure. Similarly, at different critical states corresponding to various inlet gauge pressures, the relationship with the leakage rate is nearly linear in the ranges of 0–30 kPa and 60–300 kPa. However, between 30 and 60 kPa, the leakage rate exhibits a

sudden increase. This is actually a symmetrical relationship around an inlet gauge pressure of approximately 48 kPa. Below 48 kPa, there is a sharp decrease in the pumping rate, while above 48 kPa, there is a sharp increase in the leakage rate, with both sides having nearly the same magnitude. At an inlet gauge pressure of approximately 48 kPa, the leakage rate is almost zero, and the critical rotational speed is approximately 14 r/min. This pressure can be referred to as "boundary-line pressure," similar to boundary-line speed, indicating the point where the leakage direction changes. It is the boundary-line at which the leakage rate transitions between leakage and pumping when other parameters remain constant. In seal design, attention must be paid to the boundary-line pressure to optimise performance and prevent undesired leakage or pumping effects.

From Equation (1), it is evident that as the inlet gauge pressure increases, the closing force increases linearly, and the corresponding film opening force also increases linearly. Therefore, the critical rotational speed follows a similar upward trend, as a higher rotational speed is required to generate sufficient film opening force to balance the forces and reach the critical opening state. Additionally, the increase in leakage rate can be explained by the greater pressure difference between the inside and outside of the seal system, which enhances the driving force for the two-phase fluid to flow through the leakage channel.

3.4.3. Influence of Temperature on Start-Up Performance

Taking the data from both Tables 1 and 2 for an inlet with a gauge pressure of 100 kPa, an oil–gas ratio of 0.03, and temperatures incrementally increasing from 40 °C to 130 °C, the variations in critical rotational speed and leakage rate were calculated. The results are presented in Figure 13.
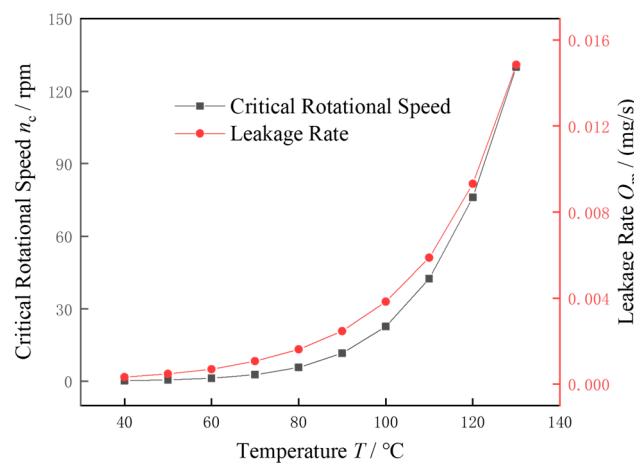

Figure 13. Critical rotational speed and leakage rate at different temperatures.

Figure 13 demonstrates that temperature has a significant impact on the start-up performance of the sealing system. Both the critical rotational speed and the leakage rate show a clear upward trend as the temperature increases. In the lower temperature range, such as from 40 °C to 80 °C, the changes in critical rotational speed and leakage rate are relatively gradual. However, as the temperature continues to rise, particularly beyond 100 °C, the increases in both parameters become more pronounced, with the curves steepening. This behaviour can be attributed to higher temperatures reducing the equivalent viscosity of the oil–gas mixture, thereby enhancing its fluidity and significantly increasing the leakage rate. Additionally, higher temperatures decrease the stiffness of the oil–gas two-phase film, reducing its load-bearing capacity. As a result, higher rotational speeds are required to reach the critical state for the seal.

In the cooling systems of electric spindles in new energy vehicles, the coolant temperature is typically controlled within the range of 40 °C to 70 °C. Some high-performance electric spindles may allow the coolant temperature to approach 80 °C, but this usually

requires more efficient cooling designs to ensure that critical components, such as bearings and motor stators, are not adversely affected. In contrast, the temperature range for traditional automotive cooling systems is generally between 75 °C and 105 °C. This suggests that this new type of seal is more suitable for new energy vehicles than for traditional vehicles. Moreover, in the lower temperature range, the corresponding critical rotational speed is lower, making the start-up process of this seal in new energy vehicles easier, shorter, and with less impact from rubbing during start-up.

4. Conclusions

Through in-depth analyses of the start-up process for high-speed micro-grooved pumping seals in new energy vehicles, this study revealed the impact of various operating parameters on sealing performance.

Firstly, when the film thickness was below the critical value, the film opening force was calculated as the difference between the closing force and the surface contact force. Changes in the fractal dimension and characteristic length scale influenced the initial film thickness. When the film thickness exceeded the critical value, the balance between the film opening force and the closing force caused the film thickness to increase non-linearly with rotational speed, reflecting a decrease in the stiffness of the oil–gas two-phase film. This further highlighted the trend of leakage rate changes at high rotational speeds. Notably, the study found that under the given operating conditions, as the rotational speed increased, the sealing system transitioned from a leakage state to a pumping state, with a boundary-line speed of approximately 102 r/min. This finding provided important operational references for the practical application of sealing systems.

Additionally, operating parameters such as oil–gas ratio, inlet gauge pressure, and temperature significantly affected the critical state. Changes in the oil–gas ratio showed a non-linear decrease in critical rotational speed, suggesting that the design process should avoid an oil–gas ratio near 0.06 to reduce leakage rates during start-up. Variations in inlet gauge pressure also affected the critical rotational speed, with a sharp increase in leakage rate and a change in leakage direction near the boundary-line pressure, which was 48 kPa under the given conditions. The influence of temperature was evident in the significant rise in both critical rotational speed and leakage rate, emphasising the importance of temperature control in the cooling systems of new energy vehicles.

In summary, this study provided a systematic theoretical foundation and guidance for optimising the start-up process of high-speed micro-grooved pumping seals in new energy vehicles. Future research could further explore the dynamic sealing performance after opening and the microscale porosity leakage in the stationary state before start-up, with the goal of achieving more efficient seal designs.

Author Contributions: Conceptualisation: H.C., X.D. and R.Y.; methodology: H.C., X.D. and R.Y.; software: H.C. and R.Y.; validation: H.C.; formal analysis: H.C.; investigation: X.H. and X.B.; resources: X.D., R.Y., X.H. and X.B.; data curation: H.C.; writing—original draft preparation: H.C.; writing—review and editing: H.C.; visualisation: H.C.; supervision: X.D. and R.Y.; project administration: H.C., X.D. and R.Y.; funding acquisition: X.D. All authors have read and agreed to the published version of the manuscript.

Data Availability Statement: Data are contained within this article.

References

1. Jeremias, G.; Simon, F.; Frank, B. Wear on radial lip seals: A numerical study of the influence on the sealing mechanism. *Wear* **2021**, *476*, 203674.
2. Wen, C.Y.; Yang, A.S.; Huang, F.J.; Chang, H.T. New deflected-helix ribbed lip seal with enhanced sealing performance. *Tribol. Int.* **2011**, *44*, 2067–2073. [CrossRef]
3. Choi, H.J.; Park, C.W.; Lee, J.C.; Kim, J.G.; Choi, S.D. Analysis on the mechanical characteristics of PTFE oil seal for the rear part in the automotive engine. *Int. J. Precis. Eng. Manuf.* **2011**, *12*, 485–490. [CrossRef]
4. Huang, T.C.; Lin, C.Y.; Liao, K.C. Sealing performance assessments of PTFE rotary lip seals based on the elasto-hydrodynamic analysis with the modified archard wear model. *Tribol. Int.* **2022**, *176*, 107917. [CrossRef]
5. Mei, B.F.; Hu, B. Development and experimental research of a new type of low friction engine oil seal. *China Auto.* **2022**, *5*, 44–48.
6. Zhmud, B.; Najjari, M.; Brodmann, B. The effects of the lubricant properties and surface finish characteristics on the tribology of high-speed gears for EV transmissions. *Lubricants* **2024**, *12*, 112. [CrossRef]
7. Greenwood, J.A.; Williamson, J.B.P. Contact of nominally flat surfaces. *Proc. R. Soc. Lond.* **1966**, *295*, 300–319.
8. Mandelbrot, B.B. Stochastic models for the Earth's relief, the shape and the fractal dimension of the coastlines, and the number-area rule for islands. *Proc. Natl. Acad. Sci. USA* **1975**, *72*, 3825–3828. [CrossRef]
9. Johnson, K.L. *Contact Mechanics*; American Society of Mechanical Engineers: New York, NY, USA, 1985.
10. Majumdar, A.A.; Bhushan, B. Role of fractal geometry in roughness characterization and contact mechanics of surfaces. *Trans. ASME J. Tribol.* **1990**, *112*, 205–216. [CrossRef]
11. Majumdar, A.; Bhushan, B. Fractal model of elastic-plastic contact between rough surfaces. *J. Tribol. Trans. ASME* **1991**, *113*, 1–11. [CrossRef]
12. Wang, S.; Komvopoulos, K. A fractal theory of the interfacial temperature distribution in the slow sliding regime: Part I—Elastic contact and heat transfer analysis. *J. Tribol.* **1994**, *116*, 812–822. [CrossRef]
13. Dong, L.; Zhang, Y.X. Revision of M-B elastoplastic contact model. *J. Sichuan Univ. Sci. Technol.* **2001**, *2*, 4–7.
14. Ge, S.R.; Zhu, H. *Fractal of Tribology*; China Machine Press: Beijing, China, 2005.
15. Bhushan, B. The real area of contact in polymeric magnetic media—I: Critical assessment of experimental techniques. *ASLE Trans.* **2008**, *28*, 75–86. [CrossRef]
16. Bhushan, B. The real area of contact in polymeric magnetic media—II: Experimental data and analysis. *ASLE Trans.* **2008**, *28*, 181–197. [CrossRef]
17. Wei, L.; Liu, Q.H.; Zhang, P.G. Sliding friction surface contact mechanics model based on fractal theory. *J. Mech. Eng.* **2012**, *48*, 106–113. [CrossRef]
18. Ding, X.X.; Yan, R.Q.; Jia, Y.L. Construction and analysis of fractal contact mechanics model for rough surface based on base length. *Tribology* **2014**, *34*, 341–347.
19. Zhao, Y.X.; Ding, X.X.; Wang, S.P. Prediction of leakage rate and film thickness of mechanical seal based on fractal contact theory. *Lubr. Eng.* **2022**, *47*, 156–163.
20. Fukui, S.; Kaneko, R. Analysis of ultra-thin gas film lubrication based on linearized Boltzmann equation: First report—Derivation of a generalized lubrication equation including thermal creep flow. *Trans. ASME J. Tribol.* **1988**, *110*, 253. [CrossRef]
21. Gu, Y.Q. Just-lift-off phenomena and lift-off characteristics of mechanical face seals. *Petro-Chem. Equip.* **2003**, *4*, 26–29.
22. Li, S.X.; Song, B.W.; Zhang, Q.X.; Cai, J.N.; Gao, J.J. Opening characteristics of dry gas seal. *CIESC J.* **2011**, *62*, 7.
23. Fan, Y.; Song, P.Y.; Xu, H.J. Study on startup operation of dry gas seal with steam lubrication. *CIESC J.* **2020**, *71*, 3671–3680.
24. Sun, X.J.; Song, P.Y.; Mao, W.Y.; Deng, Q.G.; Xu, H.J.; Chen, W. Dynamic contact analysis of dry gas seal during start-stop process considering material properties and surface topography of seal rings. *CIESC J.* **2021**, *72*, 4279–4291.
25. Chen, H.Q.; Yan, R.Q.; Hong, X.Z.; Bao, X.; Ding, X.X. Micro-groove optimisation of high-speed inner ring micro-grooved pumping seal for new energy electric vehicles. *Processes* **2024**, *12*, 1281. [CrossRef]
26. *JB/T 11289-2012*; Specification for Dry Gas Seal. China Machine Industry Press: Beijing, China, 2012.
27. Yan, W.; Komvopoulos, K. Contact analysis of elastic-plastic fractal surfaces. *J. Appl. Phys.* **1998**, *84*, 3617–3624. [CrossRef]
28. Yan, R.Q.; Chen, H.Q.; Zhang, W.Z.; Hong, X.Z.; Bao, X.; Ding, X.X. Calculation and verification of flow field in supercritical carbon dioxide dry gas seal based on turbulent adiabatic flow model. *Tribol. Int.* **2021**, *165*, 107275. [CrossRef]
29. Wen, S.Z.; Huang, P.; Tian, Y.; Ma, L.R. *Principles of Tribology*; Tsinghua University Press: Beijing, China, 2012.